Investigation of two Rolls-Royce developmental injectors using Large Eddy Simulation and Proper Orthogonal Decomposition

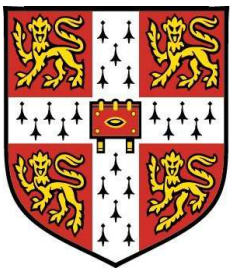

Simon Ayache

Department of Engineering

University of Cambridge

This report is a complement to the PhD thesis:

Simulations of Turbulent Swirl Combustors

Tuesday, 20^{th} of December, 2011

Acknowledgements

This work has been carried out at Rolls-Royce plc in Derby (United-Kingdom) during my PhD. I am very grateful to my supervisor, Prof. Epaminondas Mastorakos, for having arranged this valuable exchange. I am also very thankful to Dr. Marco Zedda (Rolls-Royce UK) and his CFD team for welcoming me in Derby and for making my stay there a very fruitful one. I also wish to express my gratitude to the European Commission for its financial support granted through the Marie Curie Project MYPLANET.

Abstract

This report is a complement to the PhD thesis titled *Simulations of Turbulent Swirl Combustors*. This work extends the application of the Large Eddy Simulation/Conditional Moment Closure approach developed in the thesis to flows of industrial level of geometric complexity. It has been carried out during a secondment to work at Rolls-Royce plc with the aim of sharing fundamental and applied research developments. In the PhD thesis, Proper Orthogonal Decomposition (POD) has been systematically used in order to analyze further the physics underlying the large numerical datasets obtained during the simulations. The work presented here applies these analytical methods developed in the PhD work for the academic TECFLAM burner to two lean-burn industrial injectors. POD identifies the different PVCs generated by the different swirlers composing the injector and it associates a frequency to each of them. The LES/POD analysis of industrial injectors gives results that are very consistent with the ones obtained for the TECFLAM academic burner in the PhD thesis.

Contents

List of Figures

Chapter 1

Introduction

The following work has been conducted at Rolls-Royce plc during a short placement in Derby, UK, in the Combustion Aerothermal Methods CFD team. Large eddy simulations of two lean burn development combustors had already been set-up and initialized by the CFD team. During the placement, large eddy simulations of the combustors have been restarted after several numerical probes were added at different positions inside the flow to record time-series of the velocity components and perform spectral analysis. Moreover, the simulations outputs have been recorded at constant time-step in order to perform Proper Orthogonal Decomposition of the LES datasets, for both inert and reactive simulations. In particular, the present study focuses on the hydrodynamic structures (such as the Precessing Vortex Core) generated by the multiple swirlers present in these aero-engine injectors.

Chapter 2

Motivation: lean burn combustion injectors

In this report, analysis based on Large Eddy Simulation and Proper Orthogonal Decomposition of two lean burn development injectors are presented. The new lean burn technology is based on the principle that with a higher Air-to-Fuel Ratio (AFR), the flame temperature will decrease and so will the NOx emissions. As a consequence, the aerodynamic combustor design has to change to increase the AFR ratio near the flame front, but this change also has large implications on the stability and performance of the combustor. The following description of the rich and lean burn technologies is based on discussions with Rolls-Royce engineers during the placement in Derby, UK.

In a conventional combustor, a rich diffusion flame is generated in a primary recirculation zone. This rich zone is located at the front of the combustion chamber and provides a high level of resistance to flame out. Therefore it is used to keep the combustor alight at low power conditions. Throughout large ports located along the length of the combustor, air is introduced in a transition zone that dilutes the mixture and enables most of the smoke produced in the rich zone to be consumed. Overall the combustor is running very lean. However, as the mixture passes from rich to lean mixture, there are regions of the combustor where the mixing is at stoichiometric conditions and hence NOx emissions are high.

To lower NOx emissions significantly, a new combustor has been designed to operate in lean conditions also in the front part of the combustion chamber. In this configuration, all the air, apart from the cooling air, is admitted through the fuel injector to provide a lean burn AFR condition everywhere in the combustor, which is required for low NOx emissions. As a consequence, there is no longer large air ports along the combustor walls as in a rich combustor. The lean burn injector is also found to be much larger, as almost all the air needed for the combustion process will enter the combustor through the injector.

The drawbacks of lean burn configurations is that there are issues with the flame stability at low power conditions. In particular, there is a high risk of blow out. To overcome this problem, a staged combustion is used, where different zones are created for a specific range of engine operation. At low power, fuel is supplied only through a small pilot injector while at higher power conditions more fuel is introduced through large main fuel injectors. The presence of these different injectors, each of them containing a swirler, creates a complex aerodynamics, which has to be studied in-depth in order to understand the stability of the combustor.

The work presented in this report investigates the stability of these development combustors from a hydrodynamic point of view by using low-mach number LES coupled to POD analysis of the combustors inert flows. An attempt to correlate these hydrodynamic instabilities to the combustion process is finally made for one of the two injectors.

Chapter 3

Method: models, codes and POD computations

The LES code PRECISE in its structured version has been used to resolve the flow and mixing fields of the two injectors in both inert and reactive situations. The different codes and models are described in Chapter 3 of Ref. [1] and specific details for each simulation are given in the two following sections.

3.1 Injector A

An inert LES simulation of the injector A has been parametrized by the CFD team in Derby. The simulation was then restarted to gather enough data to perform POD analysis. The LES was based on the standard Smagorinsky subgrid stress model and performed on a 3M cells mesh with a time-step of 2.0×10^{-6} s. During the placement in Derby, snapshots were recorded for every 125 time step i.e. a sampling frequency of $f_s = 4000$ Hz. 564 snapshots were saved, which gave a simulated time of 141 ms. LES data were first interpolated on a coarser mesh of 475k cells to reduce the computational load, before POD was performed using the three components of the velocity field and pressure field.

3.2 Injector B

Once again the simulations were parametrized by the CFD team of Rolls-Royce plc, in Derby, UK. Details of the initialization and validation of the large eddy simulations of Injector B have been given in Ref. [2] for both the inert and reacting cases. The large eddy simulations have been performed on a 8M cells grid. The time-step used was 5.0×10^{-6} s, which ensures a maximum CFL number of 0.91 in the inert case and 0.85 in the reacting case during the whole simulations as well as stable computations. The LES simulations were based on the dynamic Smagorinsky subgrid stress model. The combustion model is a first order CMC formulation, with a CMC grid based on $24 \times 24 \times 23 = 13248$ cells clustered close to the injector in order to capture the high variation in strain rate expected here. Away from the injector, the CMC grid is very coarse as the combustion is expected to be at low strain rates, and so the flamelets are expected to experience little variations. The mixture fraction space was divided into 51 points and the chemistry used was a one-step n-heptane mechanism (see Ref. [2]). Similarly to other LES-CMC simulations presented in the thesis, the initial condition for the reactive LES simulation was the solution computed with a LES/0D-CMC formulation. For the CMC equations, the initial solution used was the burning "flamelet" obtained for $N_0 = 50$ 1/s.

During the placement in Derby, the inert simulation was restarted and outputs were recorded for every 50 time steps i.e a sampling frequency of $f_s = 4000$ Hz. 427 snapshots were used for the POD computation i.e. a time interval of 106 ms. In order to perform POD, LES data were first interpolated on a coarser mesh of 945k cells, and then POD was performed using the three components of the velocity field and the mixture fraction field. Regarding the reactive case, 244 snapshots were recorded i.e. a time interval of 61 ms. POD computation of the reactive flow was based on the same variables as for the inert flow plus the temperature field.

Chapter 4

Results and Discussion

4.1 Inert flow of the Injector A

4.1.1 Overview of the flow

In Fig. 4.1, the instantaneous normalized axial velocity (left) and normalized pressure (right) contours are reproduced as well as their time-averaged counterparts, with the black line representing the zero axial velocity isoline. The injector geometry has been hidden for confidentiality reasons. In Figs. 4.1(a) and 4.1(c), the different jets from the different swirler of the injector are visible. A large CRZ, developing at the exit of the pilot (central jet) occupies most of the combustion chamber. Inside the pilot swirler, the pressure drops to values as low as -3000 Pa (not shown here) as a result of the strong swirl imposed to the flow, and remains low around the pilot exit (Figs. 4.1(b) and 4.1(d)). Figure 4.2 shows an isosurface of low pressure (-3000 Pa) at the exit of the injector, which reveals the presence of a Precessing Vortex Core developing inside the annulus of the pilot injector.

4.1.2 Velocity spectra

Figure 4.3 shows the positions of different numerical probes inside the Injector A inert flow for which the three components of the velocity have been recorded. Probes 1 and 2 are located inside the pilot swirler, which has been hidden for

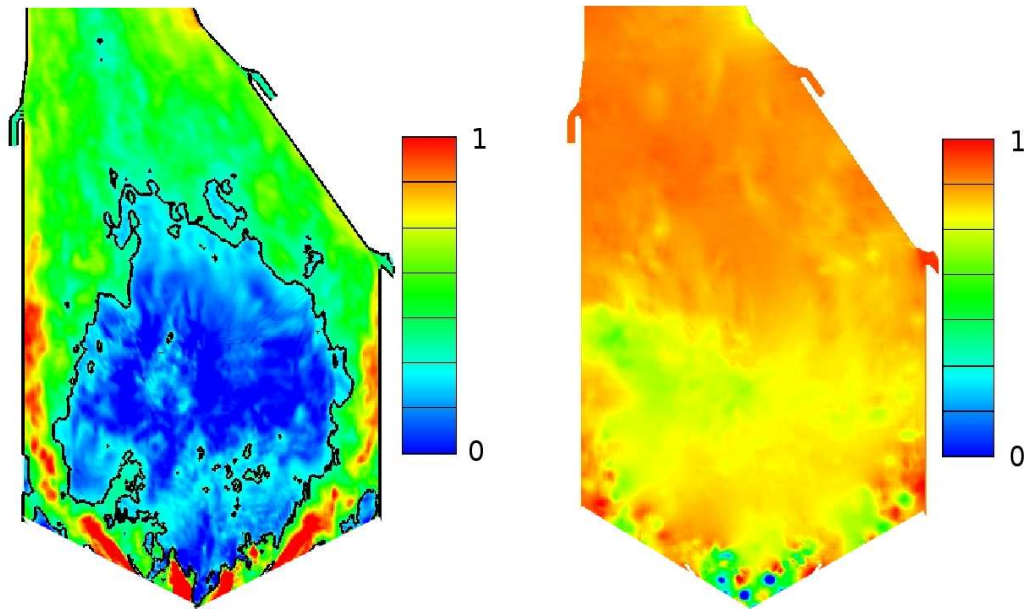

(a) Axial velocity

(b) Pressure

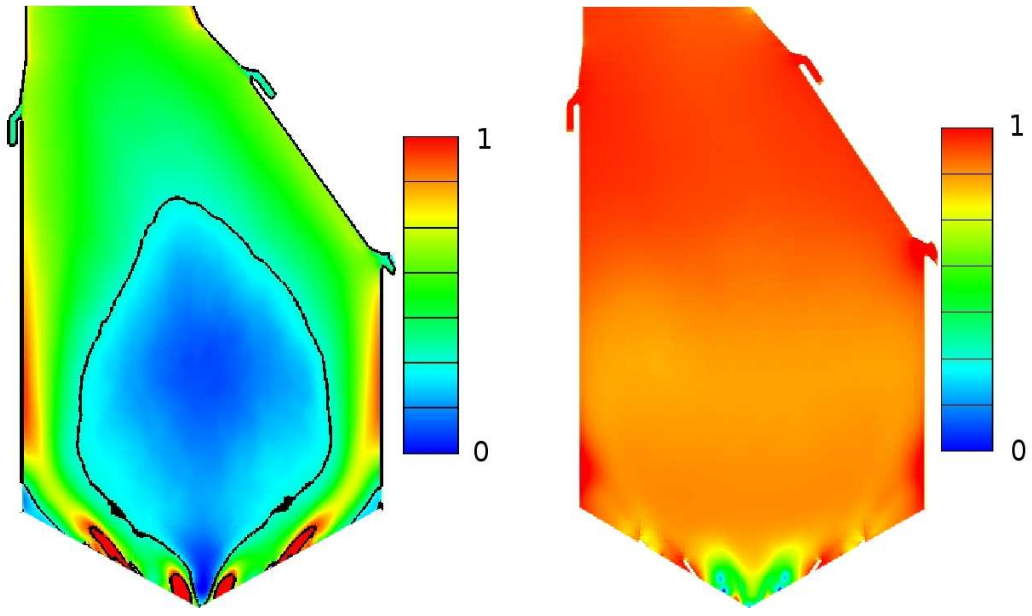

(c) Axial velocity

(d) Pressure

Figure 4.1: Inert flow of the Injector A. (a, b) Instantaneous contours of (a) the normalized axial velocity and (b) the normalized pressure. (c, d) Time-averaged contours of (c) the normalized axial velocity and (d) the normalized pressure. The black lines represent the zero axial velocity isoline.

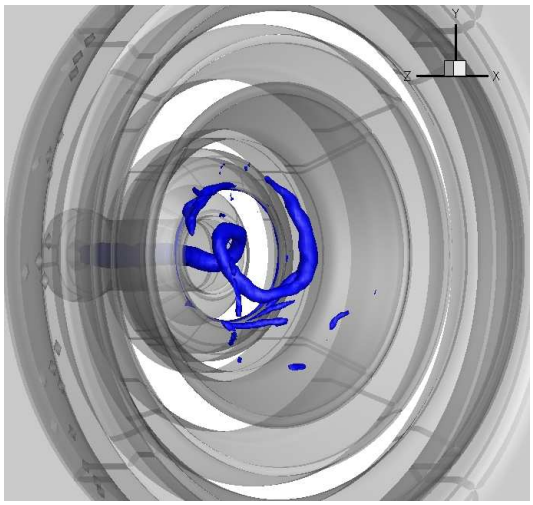

Figure 4.2: Inert flow of the Injector A. Instantaneous isosurface of low-presure (-3000 Pa).

confidentiality reasons. Figures 4.4 and 4.5 show the spectra of the axial velocity fluctuations computed over 131 ms and 65536 points. At the bottom of the pilot injector (probe 1, Fig. 4.4), spectral analysis of the axial velocity time-series reveals a high frequency of 7179 Hz. Further downstream, at an averaged distance between the injector inlet and exit (probe 2, Fig. 4.4), another strong frequency peak appears at 553.4 Hz, while the previous frequency at 7179 Hz remains the strongest one. Small frequency peaks at 2673 Hz, 4506 Hz and 5059 Hz are also present in the flow. Both probes 3 and 5 (Fig. 4.4) exhibit a clear peak at 2673 Hz and 2666 Hz respectively. Both probes are located at the pilot (central stream) exit, with probe 5 being located in the pilot jet while probe 3 is located at the front end of the CRZ. Compared to probe 3, probe 8 (Fig. 4.5) is located further downstream at a position where the CRZ has extended. It shows strong frequency peaks at 107.8 Hz, 186.9 Hz and 553.4 Hz, with smaller peaks at 43.12 Hz and 273.1 Hz. In the center of the CRZ (probe 9, Fig. 4.5), several strong frequency peaks are visible at 44.77 Hz, 104.5 Hz and a smaller one at 522.4 Hz. Towards the exit of the combustor (probe 10, Fig. 4.5), spectral analysis shows a strong frequency peak at 74.6 Hz and a smaller one at 164.2 Hz. A general observation from the different probes reported above is that the

spectra of the axial velocity exhibit high frequency close to the exit of the injector before the frequencies of the axial velocity decrease as we go further downstream. We thus find frequencies as high as 7000 Hz inside the pipe of the pilot injector, decreasing to around 2700 Hz at its exit, then around 500 Hz in the CRZ, before finally reaching around 100 Hz towards the combustor exit.

In addition to the previous probes that show relatively clear frequency peaks, probes 4, 6 (Fig. 4.4) and 7 (Fig. 4.5) exhibit spectra with a large range of frequencies. The particular feature of these probes is that they are located at positions intersected by the shear layers from the injectors jets. Probe 4 is thus located between the interface of the pilot jet and the CRZ, close the injector exit. From the frequency spectra, several frequency peaks can be observed at 179.7 Hz, 783 Hz, 1301 Hz, 1782 Hz, 2005 Hz, 2113 Hz, 2666 Hz, 3687 Hz, 4298 Hz, 5340 Hz and 6080 Hz, the strongest peaks being at 2113 Hz. Probe 6 is located in the shear layer between two main injectors streams and shows peaks at 215.6 Hz, 438.4 Hz, 740.2 Hz (strongest peak), 1775 Hz, 3004 Hz, 3701 Hz and 4082 Hz. Finally, probe 7 is located between the main jet and the outer flow along the combustor wall and exhibits frequency peaks at 96.4 Hz, 474.3 Hz, 1035 Hz, 1459 Hz (strongest peak), 1603 Hz, 3507 Hz and 5102 Hz among others.

Figure 4.6 shows the previous spectra in log-log scale to give an alternative perspective.

4.1.3 Proper Orthogonal Decomposition

As in the academic TECFLAM case presented in Chapter 6 of Ref. [1], POD has been applied to the LES dataset to further understand the dynamics of inert flow in the combustor. Here we present the first 10 modes from the analysis. Figure 4.7 represents the relative energy contained by the modes, while Figs. 4.8 to 4.13 show the different spatial modes and the spectra of their associated temporal coefficients.

Mode 1 contains 30.8 % of the energy contained in the fluctuations (Fig. 4.7). It is visualized in Fig. 4.8 by an axial velocity map at $x = 7$ mm above the injector exit (Fig. 4.8(a)) and by two isosurfaces of the axial velocity (Fig. 4.8(b), with the blue colour corresponding to negative fluctuations and the red

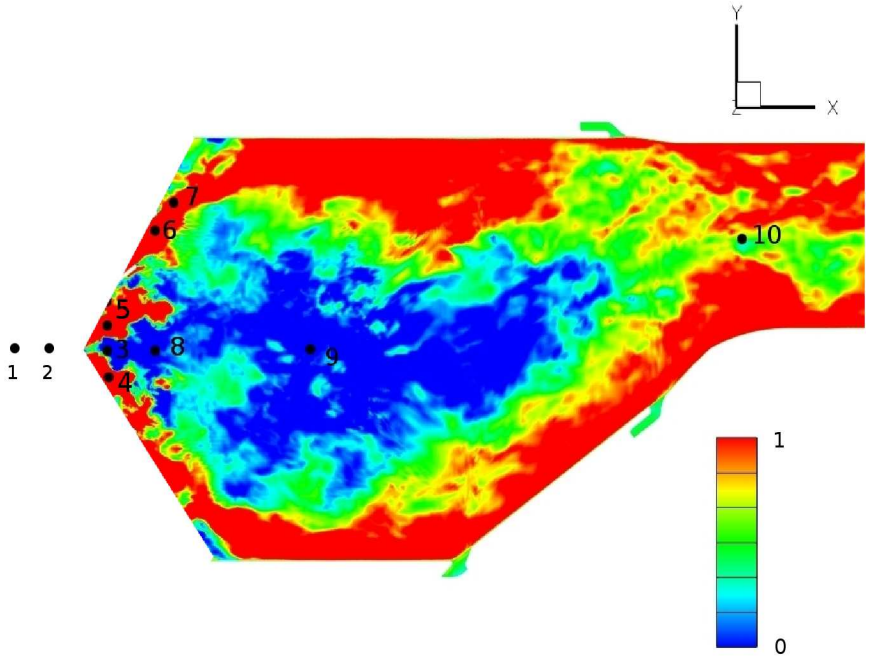

Figure 4.3: Inert flow of the Injector A. Positions of the probes superimposed on the instantaneous normalized axial velocity field.

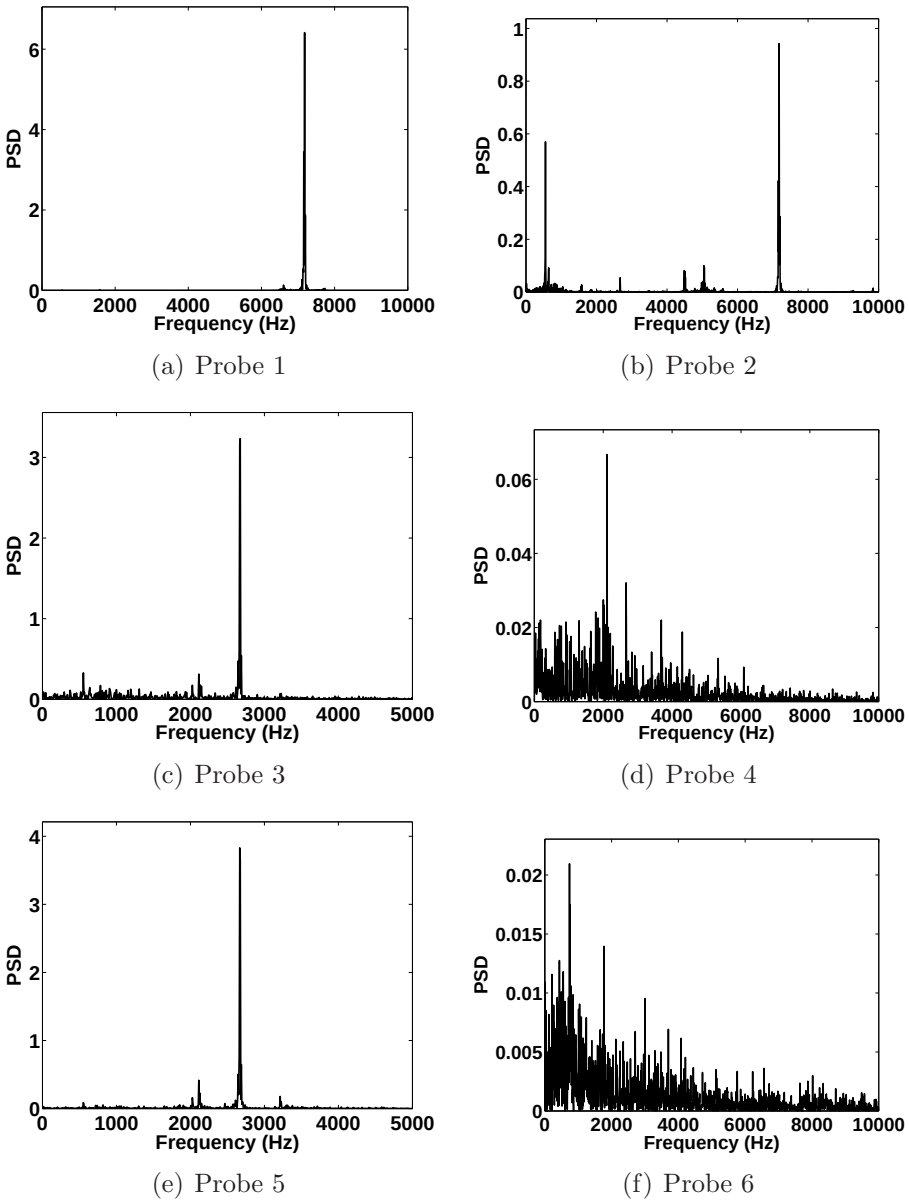

(a) Probe 1 (b) Probe 2

(c) Probe 3 (d) Probe 4

(e) Probe 5 (f) Probe 6

Figure 4.4: Inert flow of the Injector A. Spectra of the axial velocity at the positions indicated in Fig. 4.3.

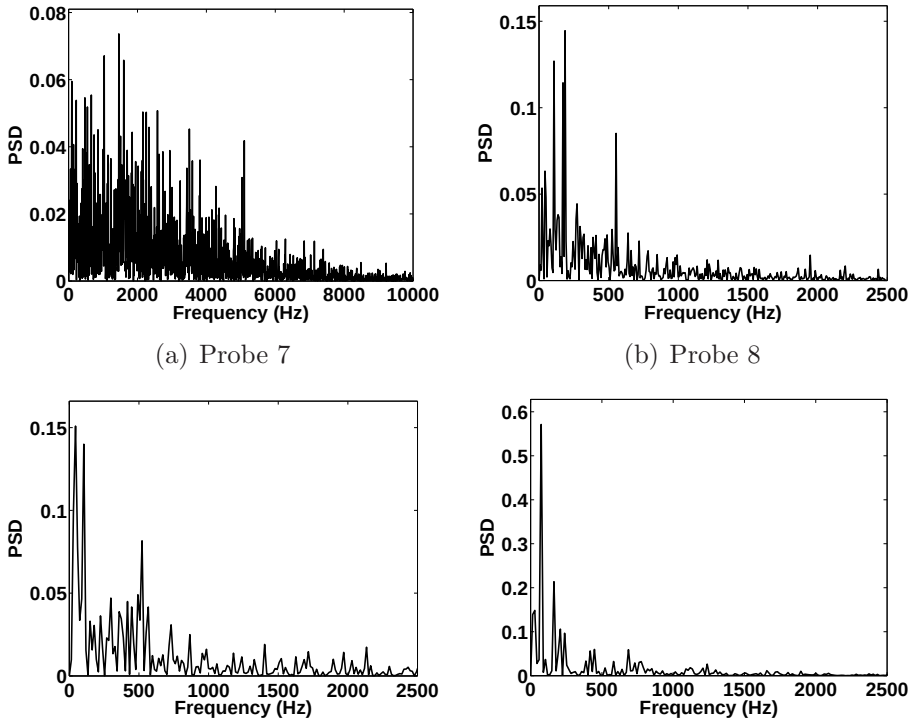

(a) Probe 7

(b) Probe 8

(c) Probe 9

(d) Probe 10

Figure 4.5: Inert flow of the Injector A. Spectra of the axial velocity at the positions indicated in Fig. 4.3.

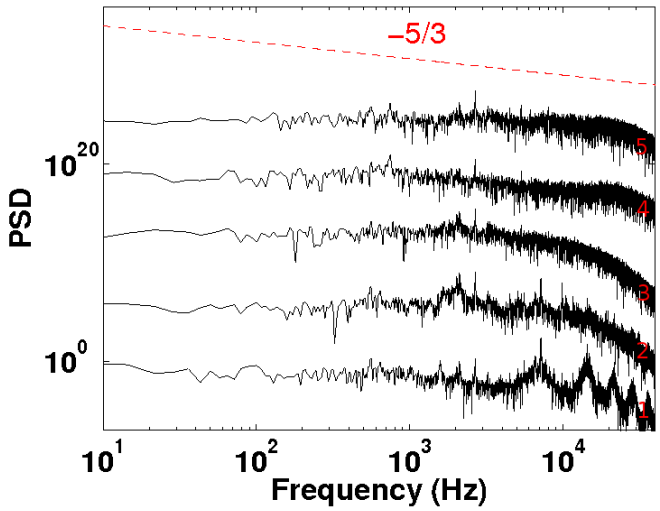

(a)

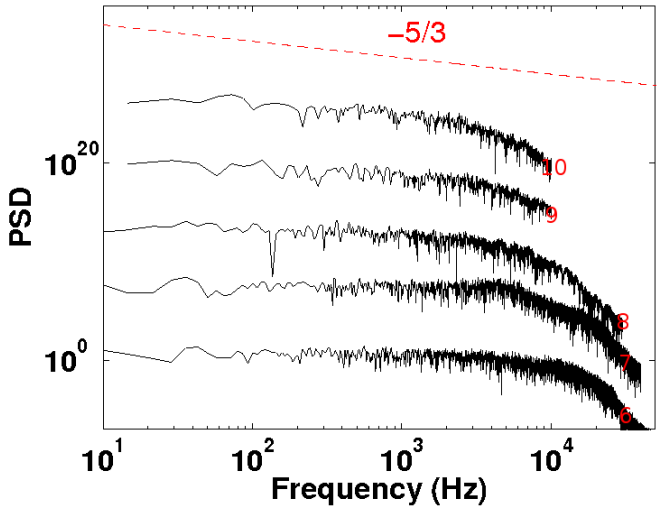

(b)

Figure 4.6: Inert flow of the Injector A. Spectra in log-log format of the axial velocity fluctuations at the positions indicated in Fig. 4.3. (a) From bottom to top: points 1 to 5. (b) From bottom to top: points 6 to 10.

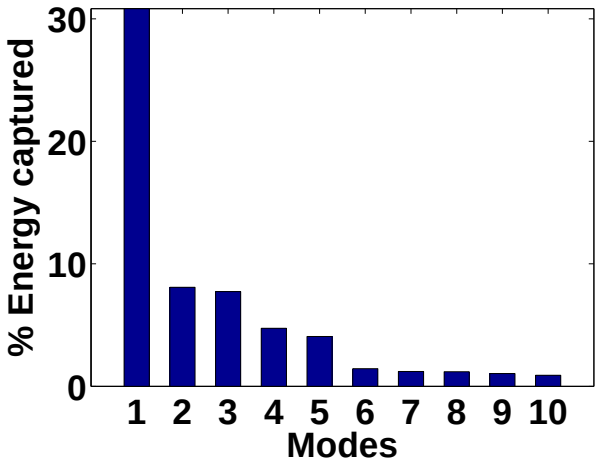

Figure 4.7: Inert flow of the Injector A. Relative energy contained by each of the first 10 POD modes.

colour to positive ones). The spectra associated with mode 1 contains a wide range of frequencies with a dominant peak at 489.4 Hz. This mode is probably associated with some axial displacement of the flow. However, the fact that the spatial mode is not axisymmetric and that its associated spectra is very noisy seems to indicate a bad convergence of the statistics. To confirm this, one needs a longer samples collected over a longer period of time.

Modes 2 and 3 form a nice pair of modes. Mode 2 contains 8.08 % and mode 3 contains 7.73 % of the total energy in the fluctuations (Fig. 4.7). Both Figs. 4.9(a) and 4.9(b) represent positive and negative isosurfaces of the pressure fluctuations. In both figures, a single helical vortex is visible inside the pilot swirler pipe, characterized by both a negative and positive pressure fluctuation isosurfaces due to vorticity conservation (or mass conservation). The spectra of modes 2 and 3 are almost identical, with a strong peak at 1333 Hz and a much smaller one at 1213 Hz. As a result, modes 2 and 3 account for the precession of a single helical vortex core at a frequency around 1333 Hz, and the PVC of the pilot swirler is found to account for 15.81 % of the total fluctuation energy of the inert combustor flow.

Looking now at modes 4 and 5 (Fig. 4.10), their representation and interpre-

tation are similar to the one just made for modes 2 and 3. This time the pair of modes account for the precession of a double helical vortex generated by the first of the main swirlers (counted from the pilot swirler along the centreline) and precessing at a frequency around 723 Hz. Another smaller frequency at 681 Hz is also present in the temporal coefficients spectra. The PVC induced by this main swirler account for $4.74 + 4.07 = 8.81$ % of the fluctuation energy in the combustor (Fig. 4.7).

Similarly to mode 1, mode 6 (Fig. 4.11) is represented by two isosurfaces of negative and positive axial velocity fluctuations. This mode may also account for an axial displacement of the flow as mode 1, with frequency peaks at 496.5 Hz, 553 Hz (strongest peak), 645 Hz and 1021 Hz. Its relative energy is found to be 1.45 % of the total energy (Fig. 4.7).

Modes 7, 8, 9 and 10 exhibit similar characteristics each other. Modes 7 and 8 (Fig. 4.12), and modes 9 and 10 (Fig. 4.13) seem to correspond respectively to a pair of modes. However, these pairs of modes appear to be noisy, probably due to their relative weakness compared to the total flow fluctuations: mode 7 relative energy accounts for 1.21 % of the total energy, mode 8 accounts for 1.19 %, mode 9 for 1.04 % and mode 10 for 0.905 % (Fig. 4.7). This is confirmed when analyzing the spectra of these four modes. Unlike a real pair of modes, modes 7 and 8 exhibit differences in their spectra. A strong frequency peak is common to both modes 7 and 8 at 439.7 Hz (strongest peak in mode 8, second strongest peak in mode 7). Mode 8 also shows small peaks at 170.2 Hz, 652.5 Hz and 1340 Hz among others. The second strongest peak in mode 8 is found at 482.3 Hz. Mode 7 shows a small peak at 1638 Hz and its strongest peak corresponds to a frequency of 489.4 Hz.

Looking now at modes 9 and 10 (Fig. 4.13), they show again discrepancies between each other, but both their strongest peaks are found at 489.4 Hz (as in mode 7). Mode 9 has also peaks at 106.4 Hz, 205.7 Hz and 553.2 Hz. Mode 10 shows other peaks at 92.2 Hz, 1128 Hz and 1326 Hz. As a result, it is found that these four modes exhibit their strongest frequency peak around 440 - 490 Hz. Moreover, their spacial representation (through isosurfaces of negative and positive pressure fluctuations) are similar. In fact, mode 7 and mode 8 spatial representations are only shifted by a rotation of $\pi/2$ and, although it is more

difficult to conclude for modes 9 and 10 due to the noise present in mode 10, they seem to exhibit the same features. As a consequence, modes 7, 8, 9 and 10 seem to describe the rotation of a single large helical vortex created by the second main swirler (counted from the pilot injector along the centreline) and at a frequency varying around 440 Hz - 490 Hz.

Figure 4.14 summarizes the different vortical structures identified thanks to the POD computation. Modes 2 and 3 account for a single helical PVC of the pilot swirler, modes 4 and 5 for the double helical PVC of the first main swirler, located just around the pilot pipe, and modes 7, 8, 9 and 10 account for the single helical PVC created by the second main swirler located around the first one. In this study, the POD analysis has thus be able to decompose the whole combustor inert flow into the different flows generated by each swirler, which allows us to further understand the aerodynamics created by the interaction of each swirler in the injector.

4.2 Inert flow of the Injector B

4.2.1 Overview of the flow

Figure 4.15 shows the instantaneous fields of the normalized axial velocity (Fig. 4.15(a)), normalized pressure (Fig. 4.15(b)) and mixture fraction (Fig. 4.15(c)), as well as the time-averaged normalized axial velocity (Fig. 4.15(d)) and normalized pressure (Fig. 4.15(e)). Once again, the injector geometry has been hidden for confidentiality reasons. From the normalized axial velocity fields, several jets from different swirlers of the injector are visible. A large CRZ occupies most of the combustion chamber. Unlike in the Injector A where the CRZ was developing itself only from the pilot swirler, giving to the CRZ a spades-like shape, this time the CRZ shows three branches, the central one corresponding to the pilot swirler and the outer ones being created by the main swirlers.

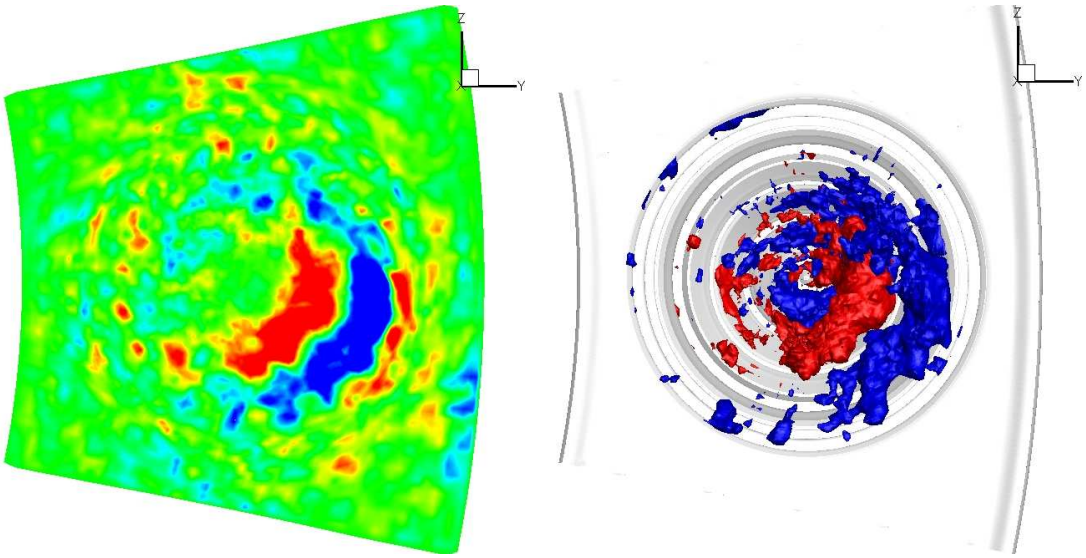

(a) U contour ($x = 7\ mm$)

(b) U isosurfaces (blue/red colours, negative/positive fluctuations)

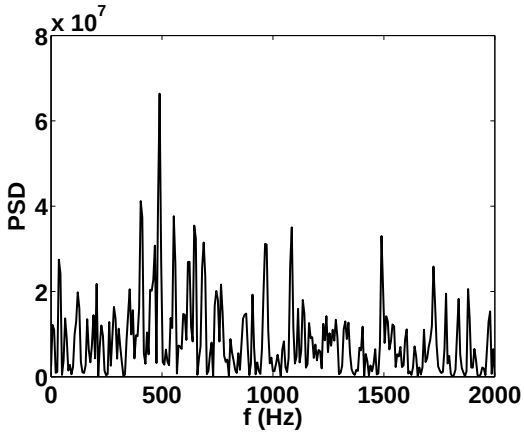

(c) Spectrum

Figure 4.8: POD mode 1 from the inert flow of the Injector A.

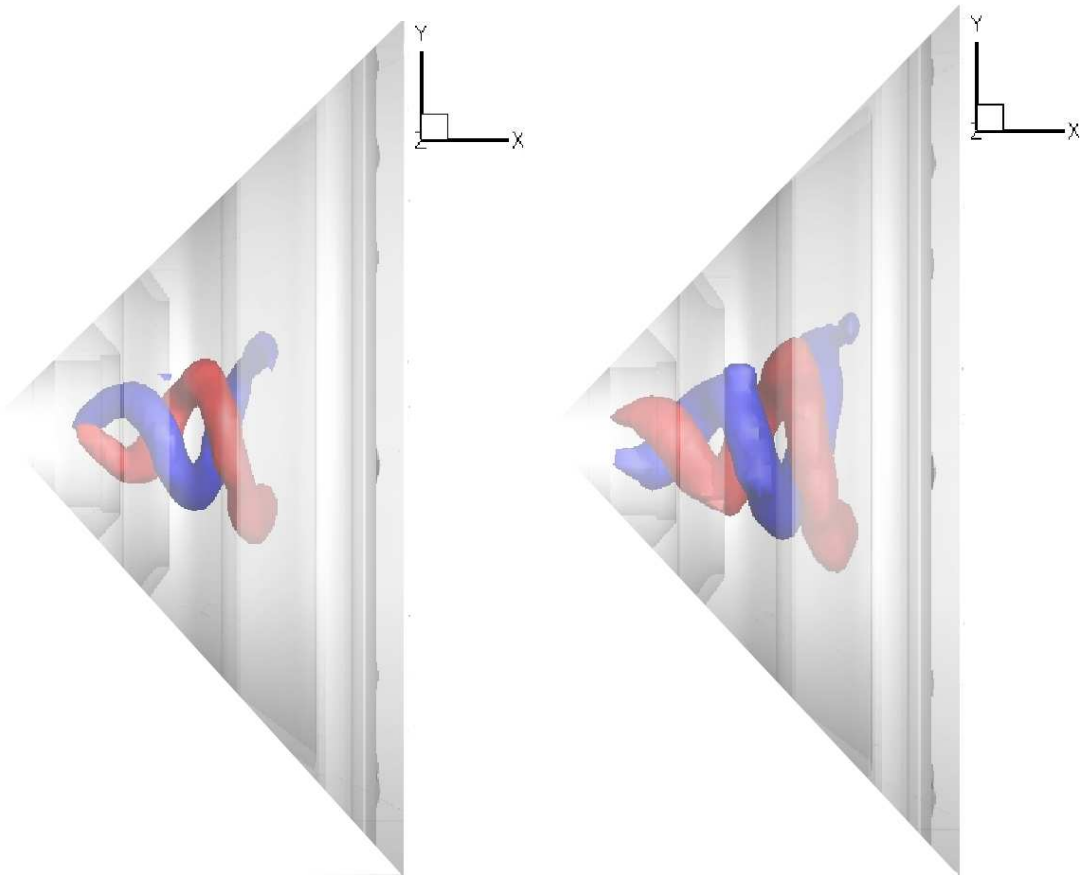

(a) Mode 2 (Q, U)

(b) Mode 3 (Q, U)

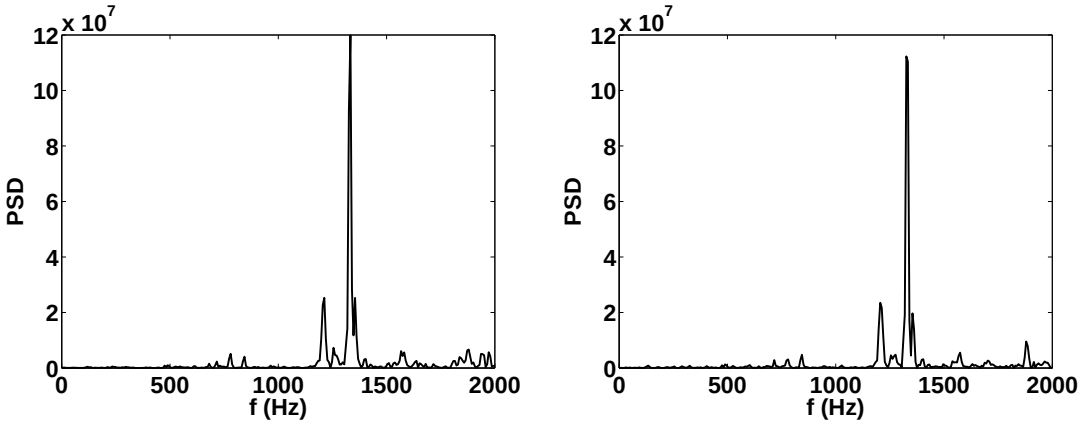

(c) Mode 2, spectrum

(d) Mode 3, spectrum

Figure 4.9: POD modes 2 and 3 from the inert flow of the Injector A.

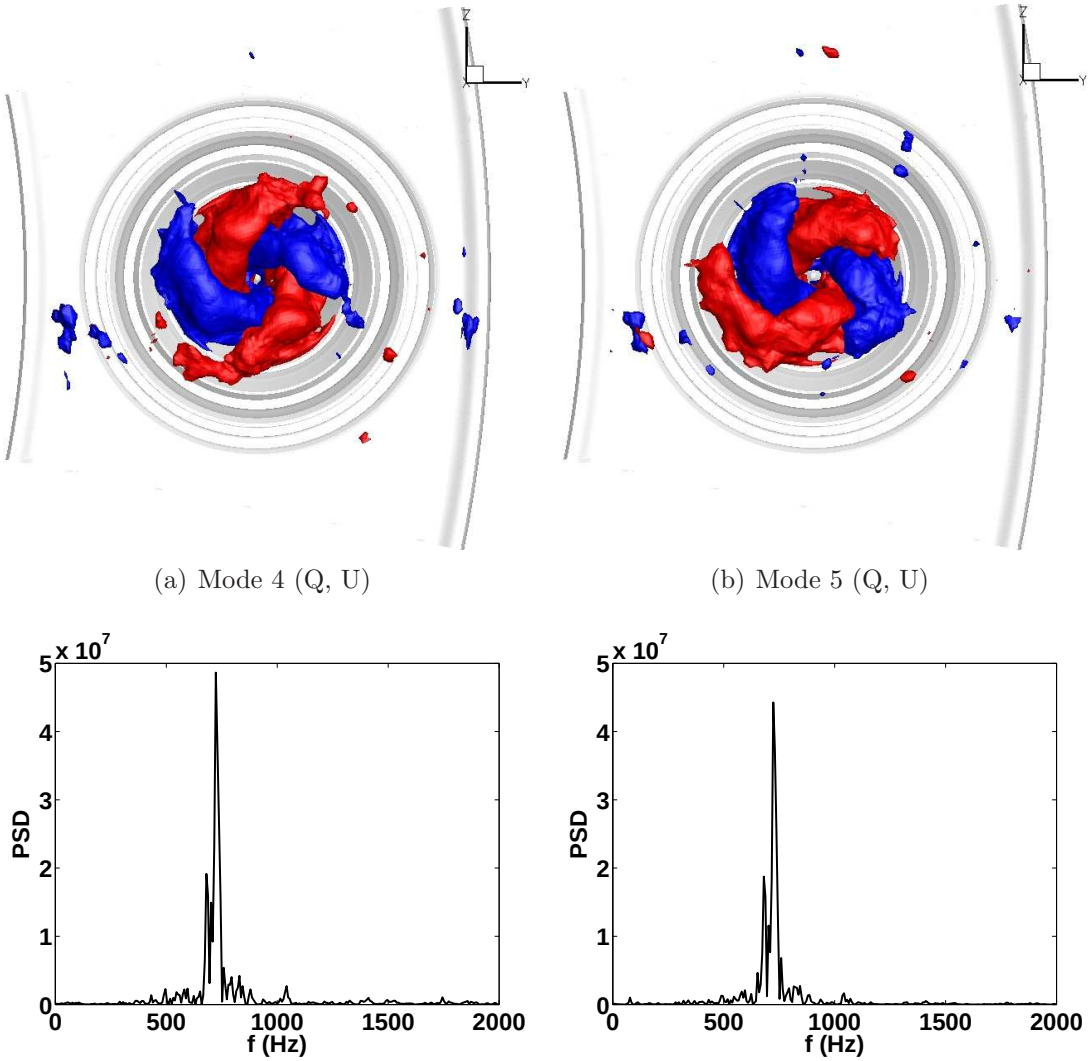

(a) Mode 4 (Q, U)

(b) Mode 5 (Q, U)

(c) Mode 4, spectrum

(d) Mode 5, spectrum

Figure 4.10: POD modes 4 and 5 from the inert flow of the Injector A.

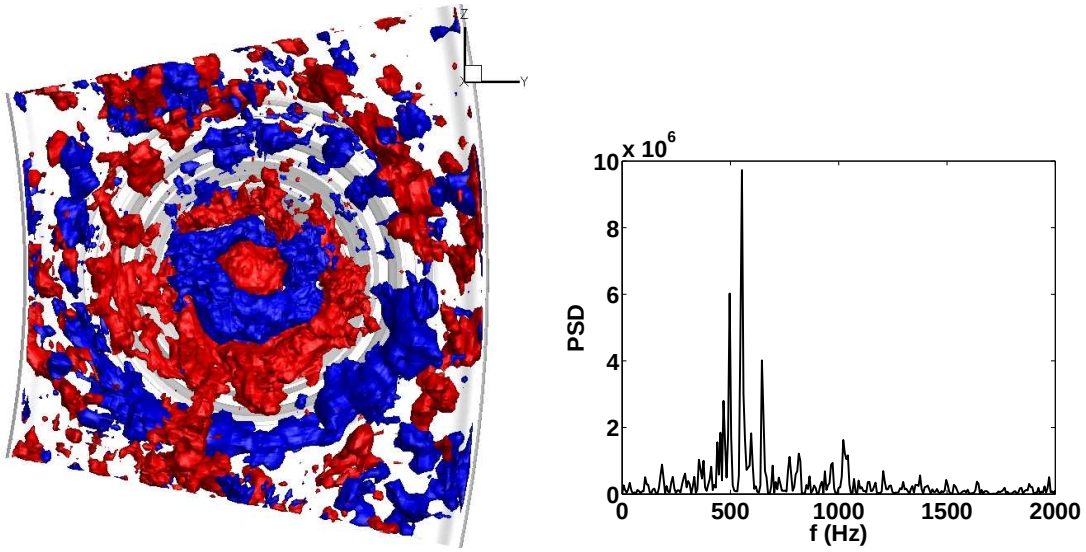

(a) U isosurfaces

(b) Mode 6, spectrum

Figure 4.11: POD mode 6 from the inert flow of the Injector A.

4.2.2 Velocity spectra

Figure 4.16 shows the locations of the different numerical probes inside the combustor while Figs. 4.17 and 4.18 show the spectral analysis of the axial velocity time series recorded by the different probes. Probe 1 is located inside the pipe of the pilot swirler, probes 2 and 3 in the CRZ, more precisely in the part created by the pilot swirler, and close to the shear layer between the pilot jet and the CRZ. Probe 4 is located inside the jet of the pilot swirler. Each spectrum of the axial velocity from these 4 probes presents similarities. The spectrum is clear (very little noise is present) and there is a strong peak at 1091 Hz. Inside the pilot swirler, very small harmonics are visible at 2182 Hz, 3273 Hz and 4364 Hz (Probe 1, Fig. 4.17(a)). Close to the shear layer between the CRZ and the pilot jet, the first harmonic at 2182 Hz has been triggered (Probe 2, Fig. 4.17(b)), while inside the part of the CRZ created by the pilot swirler (central swirler) only the fundamental frequency at 1091 Hz is visible (Probe 3, Fig. 4.17(c)). Inside the pilot jet (probe 4, Fig. 4.17(d)), the fundamental at 1091 Hz and its first harmonic at 2182 Hz are visible. Probe 5 is located into the part of the CRZ created by the main swirler. The main frequency peak is found at 116.1 Hz, with

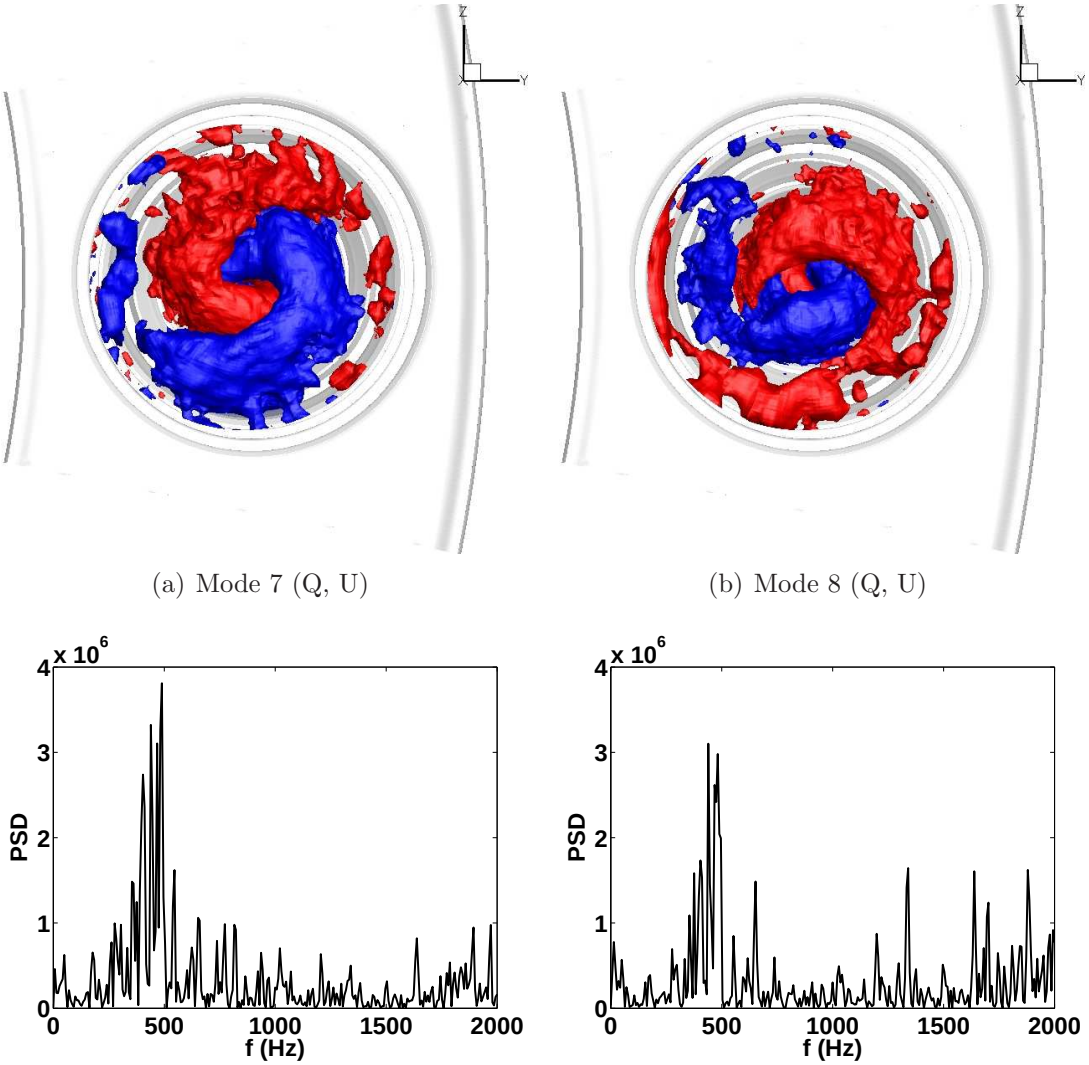

(a) Mode 7 (Q, U)

(b) Mode 8 (Q, U)

(c) Mode 7, spectrum

(d) Mode 8, spectrum

Figure 4.12: POD modes 7 and 8 from the inert flow of the Injector A.

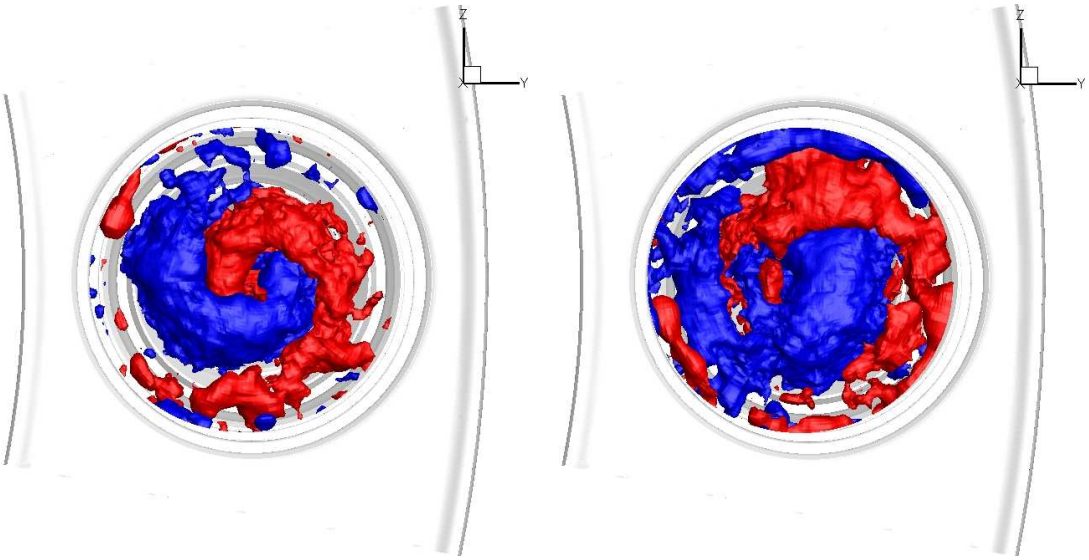

(a) Mode 9 (Q, U)

(b) Mode 10 (Q, U)

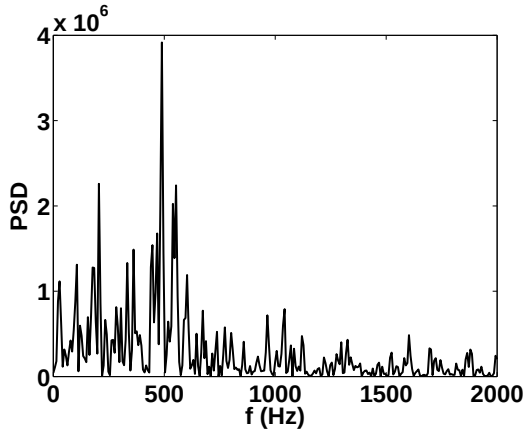

(c) Mode 9, spectrum

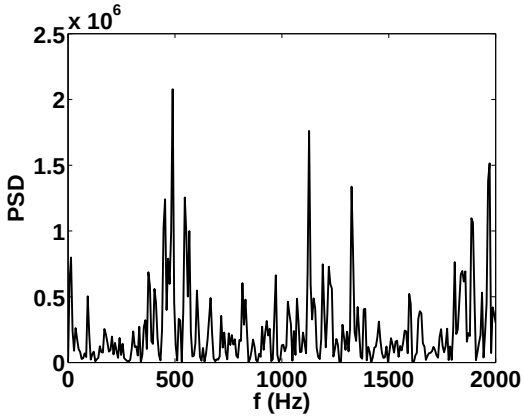

(d) Mode 10, spectrum

Figure 4.13: POD modes 9 and 10 from the inert flow of the Injector A.

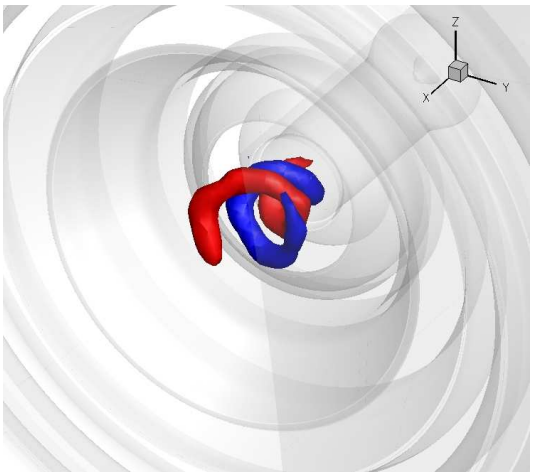

(a) PVC of the pilot swirler (modes 2 and 3)

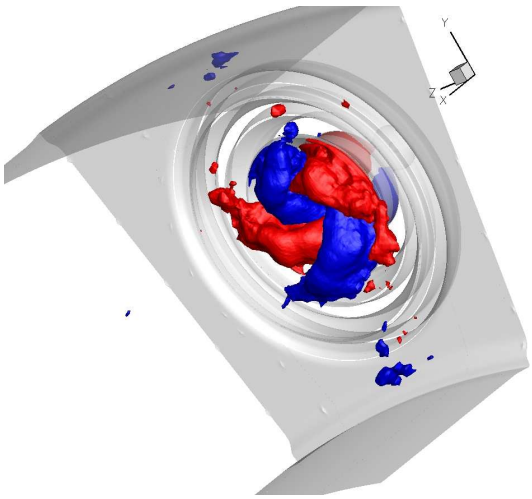

(b) PVC of the first main swirler (modes 4 and 5)

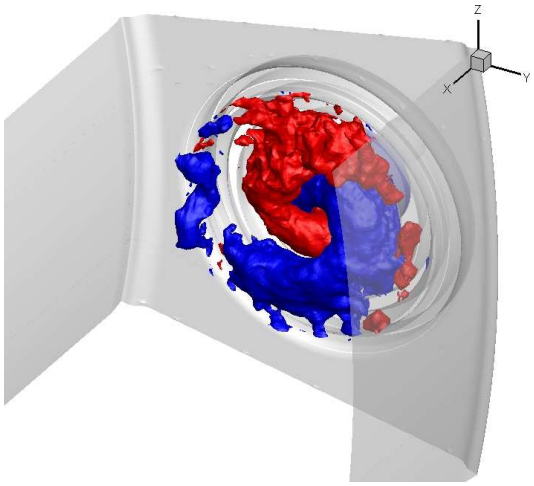

(c) PVC of the second main swirler (modes 7, 8, 9 & 10)

Figure 4.14: The different PVCs as identified by the POD analysis of the Injector A inert flow.

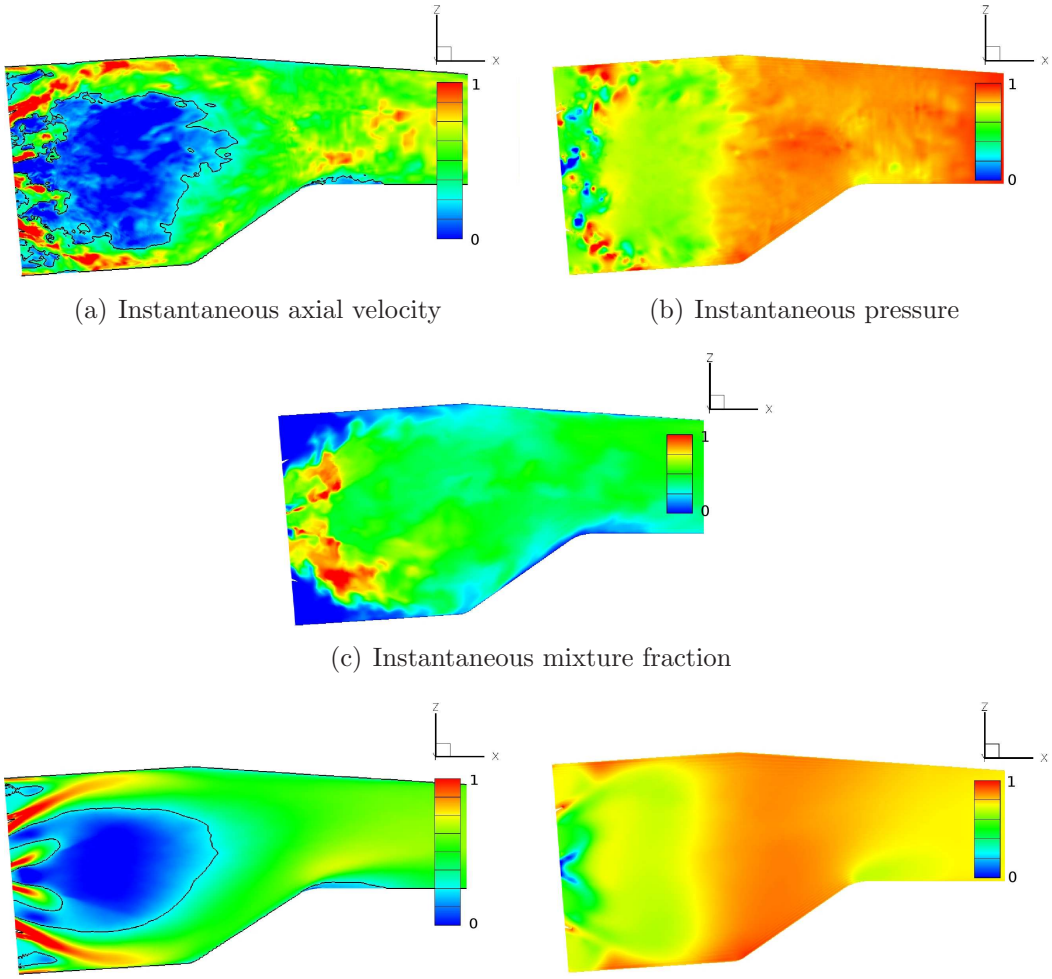

(a) Instantaneous axial velocity

(b) Instantaneous pressure

(c) Instantaneous mixture fraction

(d) Mean axial velocity

(e) Mean pressure

Figure 4.15: Inert flow of the Injector B. (a, b, c) Instantaneous contours of (a) the normalized axial velocity, (b) the normalized pressure and (c) the mixture fraction. (d, e) Time-averaged contours of (d) the normalized axial velocity and (e) the normalized pressure. The black lines represent the zero axial velocity isoline.

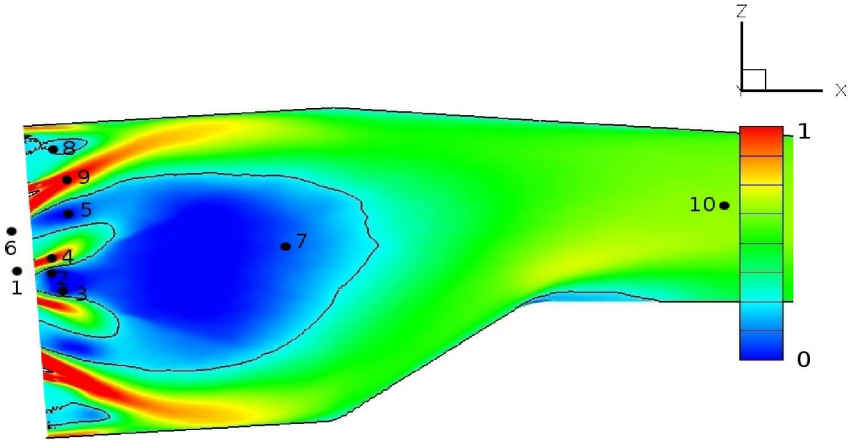

Figure 4.16: Inert flow of the Injector B. Positions of the probes superimposed on the time-averaged normalized axial velocity field. The black lines represent the zero axial velocity isoline.

secondary peaks at 220.6 Hz, 336.7 Hz, 429.5 Hz, 522.4 Hz, 1010 Hz and 1184 Hz among others. Some of these peaks may be statistical i.e. due to the noise. Probe 6 is located in the annulus of the main swirler. Its spectrum is very noisy with some strong peaks at 986.8 Hz, 2391 Hz, 9415 Hz and 9821 Hz. Inside the jet of the main swirler (probe 9), the strongest frequency observed is 1068 Hz, with other peaks at 743 Hz, 986.8 Hz and 1138 Hz among others. Inside the small RZ between the main jet and combustor walls (probe 8), frequency peaks at 58 Hz, 93 Hz (strongest peak), 209 Hz and 302 Hz are observed. In the middle of the combustion chamber, inside the CRZ (probe 7), the strongest frequency peaks are found at 34.83 Hz and 348.3 Hz, with other peaks at 150.9 Hz, 278.6 Hz, 476 Hz and 650.1 Hz also present. Towards the rear end of the combustion chamber (probe 10), a frequency of 34.83 Hz is observed. From a general point of view, the flow in the pilot swirler stream is characterized by a high frequency at 1091 Hz, while the CRZ experiences lower frequency at 34.83 Hz and 348.3 Hz. The different spectra presented here have been plotted in log-log format in Fig. 4.19.

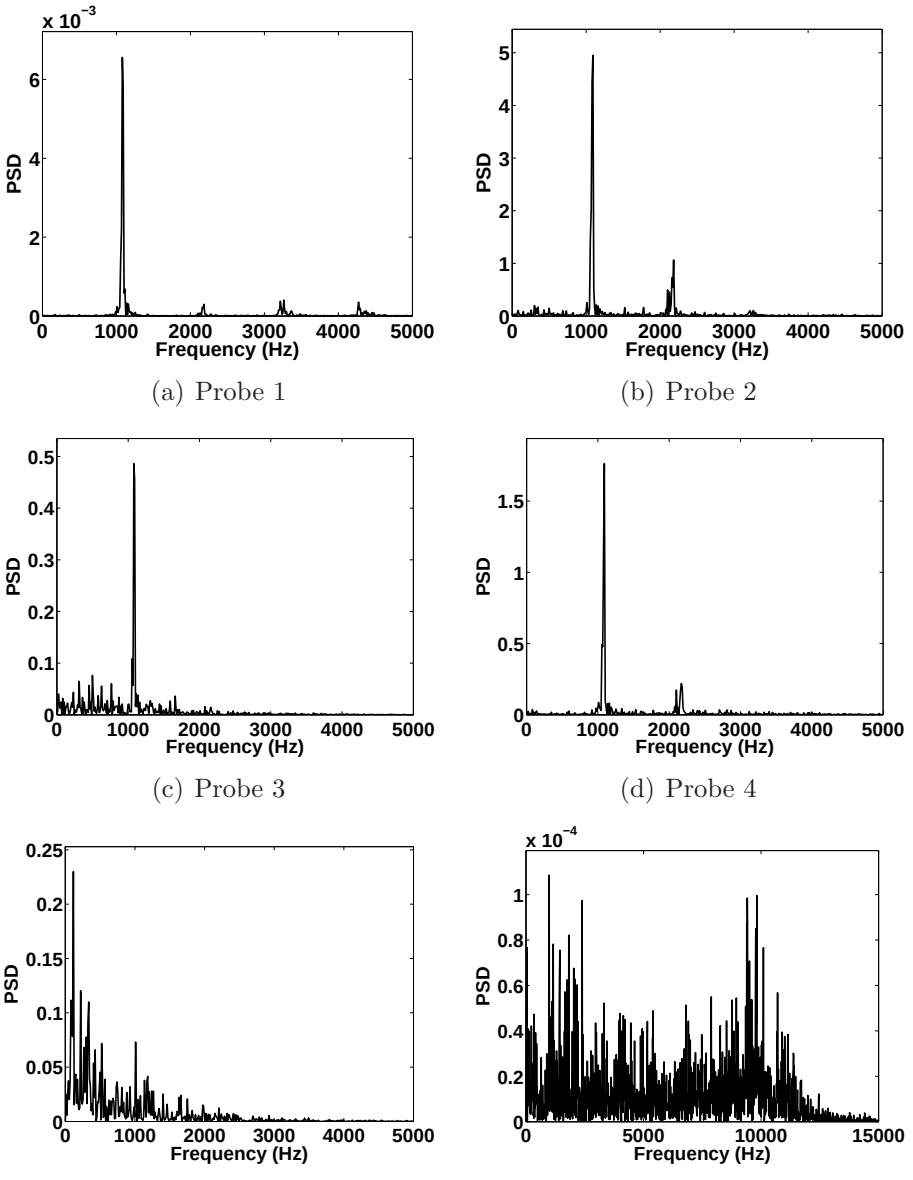

(a) Probe 1 (b) Probe 2

(c) Probe 3 (d) Probe 4

(e) Probe 5 (f) Probe 6

Figure 4.17: Inert flow of the Injector B. Spectra of the axial velocity at the positions indicated in Fig. 4.16.

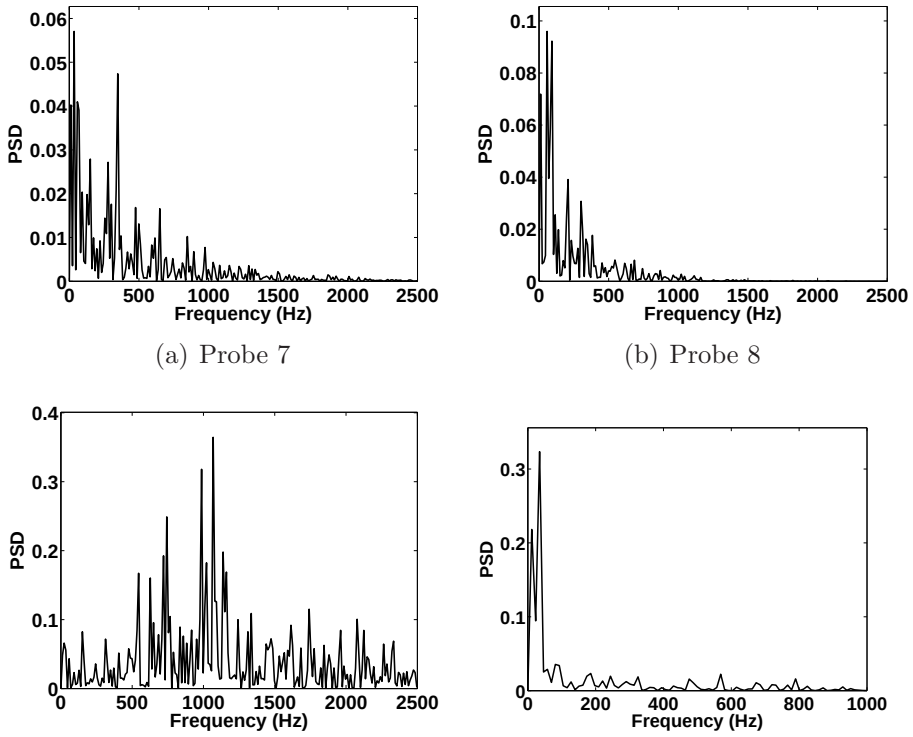

(a) Probe 7

(b) Probe 8

(c) Probe 9

(d) Probe 10

Figure 4.18: Inert flow of the Injector B. Spectra of the axial velocity at the positions indicated in Fig. 4.16.

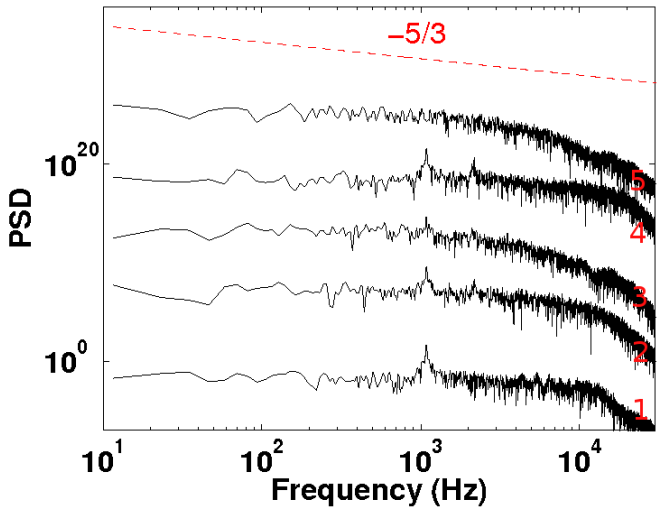

(a)

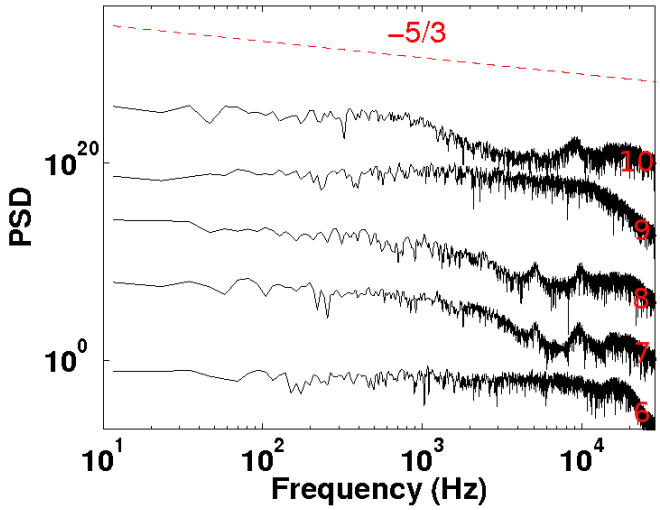

(b)

Figure 4.19: Inert flow of the Injector B. Spectra in log-log format of the axial velocity at the positions indicated in Fig. 4.16. (a) From bottom to top: points 1 to 5. (b) From bottom to top: points 6 to 10.

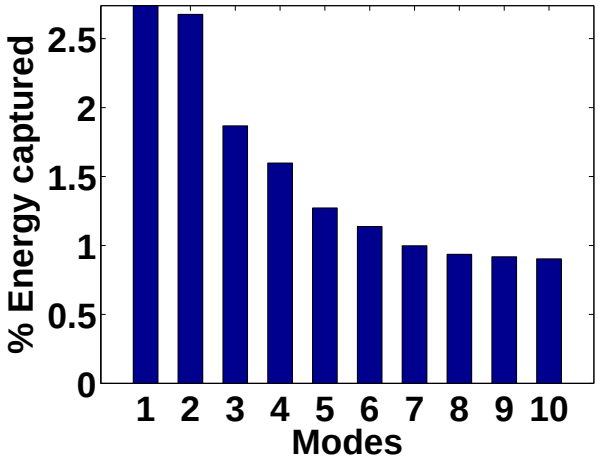

Figure 4.20: Inert flow of the Injector B. Relative energy contained by each of the first 10 modes.

4.2.3 Proper Orthogonal Decomposition

Figure 4.20 represents the energy distribution of the first 10 modes from the POD analysis of the Injector B inert flow. Modes 1 and 2 contain respectively 2.74 % and 2.68 % of the fluctuation energy and are represented in Fig. 4.21. Figures 4.21(a) and 4.21(b) represent the $Q-$criterion applied respectively to mode 1 and mode 2 and coloured by their respective axial velocity fluctuations. Figures 4.21(c) and 4.21(d) show the axial velocity fluctuations contours of mode 1 and mode 2 respectively, with two isosurfaces of the axial velocity, one negative in blue, one positive in red, superimposed on them. Both Figs. 4.21(e) and 4.21(f) show a negative (blue colour) and positive (red colour) isosurfaces of the mixture fraction fluctuations of mode 1 and mode 2 respectively. Finally, Figs. 4.21(g) and 4.21(h) represent the spectra associated with the temporal coefficients of mode 1 and mode 2 respectively. From these figures and the previous POD analysis made for the academic TECFLAM burner (Chapter 6 of Ref. [1]), it is clear that modes 1 and 2 form a pair of modes characterizing the precession of a single helical PVC at 1082 Hz, which accounts for 5.42 % of the total fluctuation energy. A close look at the roots of these vortices show that they are anchored on the bluff body surface of the pilot swirler, similarly to what was observed in

the academic TECFLAM case (Chapter 6 of Ref. [1]).

Modes 8 and 9 are represented in Fig. 4.22 in a similar way as modes 1 and 2 in Fig. 4.21. They account respectively for 0.93 % and 0.92 % of the fluctuation energy (Fig. 4.20). This pair of modes could represent the rotation of a double helical vortex PVC that accounts overall for 1.85 % of the total fluctuations. From the spectra of the temporal coefficient, it is clear that their rotation around the bluff body of the pilot injector is characterized by two frequencies at 65.57 Hz and 1852 Hz. However, it is noticeable that the roots of these vortices are located at the same place as the vortex roots of modes 1 and 2 i.e. on the top of the central bluff body of the pilot injector. The fact that they are generated by the same swirler leads to the conclusion that modes 1 and 2 on one hand, and modes 8 and 9 on another hand, could also represent the same hydrodynamic phenomenon. Despite the fact that the main frequency associated with modes 8 and 9 (1852 Hz) is lower than the first harmonic of modes 1 and 2 ($2 \times 1082 Hz = 2164$ Hz), the most logical interpretation remains that the pair of modes 8 and 9 is a harmonic of the pair of modes 1 and 2. The discrepancy with a pure harmonic case may result from some interactions with other frequencies inside the flow. It is also interesting to notice that the two pairs of modes (1, 2) and (8, 9) of this development injector inert flow are very similar to the two pairs of modes (2, 3) and (5, 6) in the case of the reactive TECFLAM burner (see Chapter 6 of Ref. [1]).

The other modes of the flow do not offer any easy interpretation and are therefore not reported in this thesis.

4.3 Reactive flow of the Injector B

4.3.1 Overview of the flow

Figure 4.23 represents the instantaneous normalized axial velocity, normalized mixture fraction and normalized temperature fields of the reactive flow of the Injector B. The normalized axial velocity contour of the reactive combustor flow (Fig. 4.23(a)) is rather different than its inert counterpart. The CRZ has experienced a dramatic shrinkage. As a result, the Recirculation Zone (RZ) created by the pilot swirl (central annulus) does not merge any longer with the RZ created

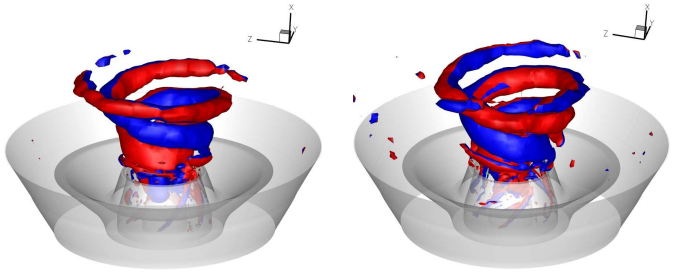

(a) Mode 1 (Q, U) (b) Mode 2 (Q, U)

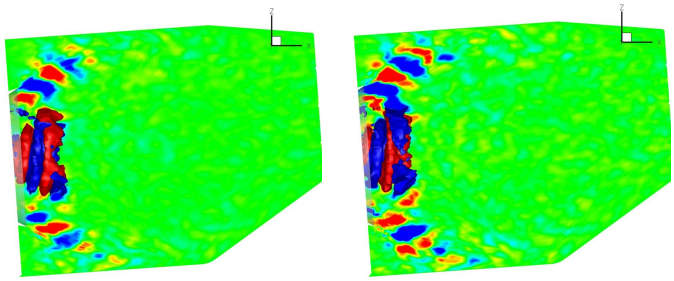

(c) Mode 1 (U) (d) Mode 2 (U)

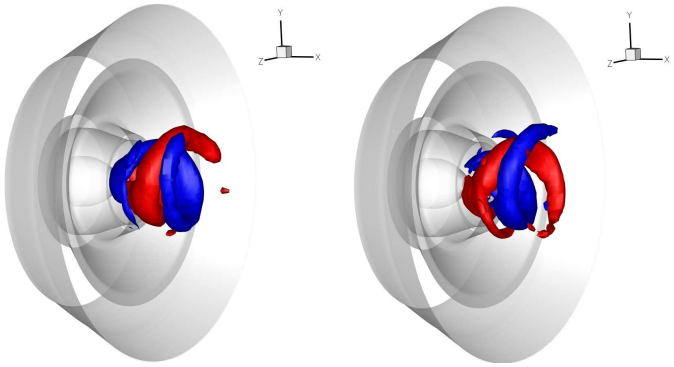

(e) Mode 1 (ξ) (f) Mode 2 (ξ)

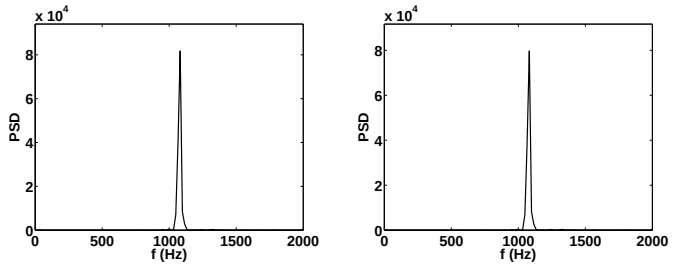

(g) Mode 1, spectrum (h) Mode 2, spectrum

Figure 4.21: POD modes 1 and 2 from the inert flow of the Injector B.

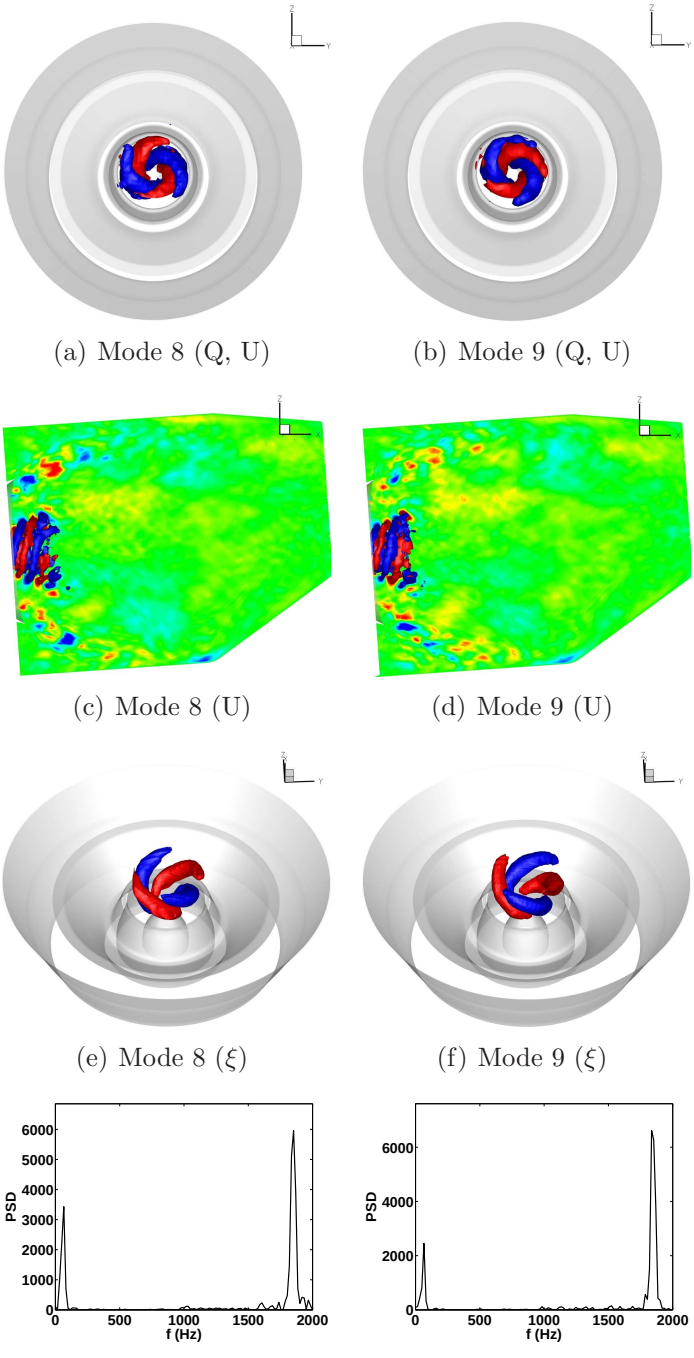

(a) Mode 8 (Q, U) (b) Mode 9 (Q, U)

(c) Mode 8 (U) (d) Mode 9 (U)

(e) Mode 8 (ξ) (f) Mode 9 (ξ)

(g) Mode 8, spectrum (h) Mode 9, spectrum

Figure 4.22: POD modes 8 and 9 from the inert flow of the Injector B.

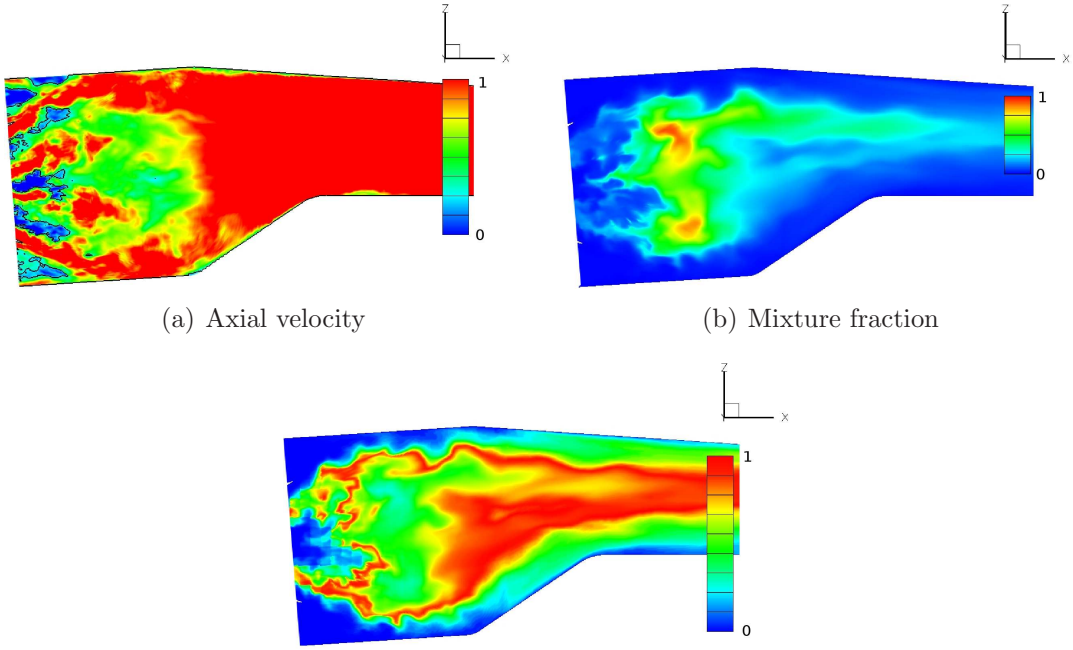

(a) Axial velocity

(b) Mixture fraction

(c) Temperature

Figure 4.23: Reactive flow of the Injector B. Instantaneous contours of (a) the normalized axial velocity, (b) the mixture fraction and (c) the normalized pressure. The black line represents the zero axial velocity isoline.

by the main swirler (outer annulus).

4.3.2 Velocity spectra

The different probes for the reactive simulation of the Injector B are located at the same positions as for the inert case (see Fig. 4.16). The different spectra are presented in Figs. 4.24 and 4.25 in their linear representations, and in Fig. 4.26 in their log-log representations. The results from the different probes in the reactive flow are qualitatively similar to the ones observed in the inert flow. Probes 1, 2, 3 and 4, which are located in the area of influence of the pilot jet, present a fundamental frequency at 1161 Hz. Harmonics at 2322 Hz (probes 1, 2, 3 and 4) and 3483 Hz (probe 4 in the pilot jet) are also visible at each of these positions, which leads again to the conclusion that the combustion tends to trigger harmonics in the flow spectra (see Chapter 6 of Ref. [1]). The strongest harmonics are found inside the pilot stream (probe 4). Another frequency at 81.76 Hz is also present in the time-series recorded by the four probes, in particular in probes 2 and 3 that are located at the RZ side of the shear layer developing between the pilot jet and the RZ created by the pilot swirler. We now look at the Power Spectral Density (PSD) values of both inert and reactive flows spectra. In one hand, spectral analysis of probe 4 in the reactive case shows a fundamental at 1161 Hz with a PSD value of 0.37 and a harmonic at 2322 Hz with a PSD value of 0.33. On the other hand, in the inert case, the spectral analysis shows a peak at 1091 Hz with a PSD value of 1.8 and a small harmonic at 2182 Hz with a PSD value of 0.22. From this observation, it is clear that the oscillations present in the flow are dramatically reduced by the combustion process, as it was previously reported for the academic TECFLAM burner in Chapter 6 of Ref. [1]. Probe 5 (located inside the RZ created by the main swirler) contains a frequency peak at 163.5 Hz and smaller peaks at 670.4 Hz and 1275 Hz. Located inside the annulus of the main swirler, probe 6 is now much less noisy than it was in the inert flow and presents a fundamental at 6017 Hz and a harmonic around 12000 Hz. Probe 7 in the reactive flow also shows very different data compared to the inert case. The reason is that probe 7 is located inside the large CRZ in the inert flow, while it is located inside the combustor stream in the reactive flow.

Its spectrum shows a strong peak at 6017 Hz as well as a smaller one at 81.76 Hz. The spectra from probes 8, 9 and 10 are qualitatively similar in both the inert and reacting cases. Probe 8 (ORZ between the main jet and the combustor walls) contains its strongest peak at 65.41 Hz and a smaller one at 261.6 Hz. Probe 4, located inside the main jet (outer swirler), has strong frequency peaks at 1177 Hz, 1374 Hz and 1504 Hz. Finally probe 10, located at the rear end of the combustion chamber, presents a frequency peak at 81.76 Hz.

4.3.3 Proper Orthogonal Decomposition

Figure 4.27 shows the energy distribution of the most energetic modes of the POD computation of the combustor reactive flow. The first 10 modes of the POD analysis have been analysed. In this thesis we reproduce the first 3 modes in Fig. 5.1 throughout their axial velocity, mixture fraction and temperature fluctuations contours, as well as the spectra of their temporal coefficients. The $Q-$criterion has also been applied to identify vortical structures. The other modes are not represented as they do not offer any physical interpretation and therefore do not help in understanding the reactive flow features.

Looking at the spectra of the first 3 modes, we note that their frequencies are rather low. Mode 1 has two characteristic frequencies at 16.39 Hz and 114.8 Hz. Mode 2 presents two frequency peaks at 32.79 Hz and 81.97 Hz. Mode 3 has a strong peak at 49.18 Hz and a small one at 131.1 Hz. Overall the POD analysis has not captured in its 10 most energetic modes any of the high frequencies that were observed in the spectral analysis of the probes. Analysis of the spectra of the probes time-series at positions located in the pilot and main jets has revealed a fundamental frequency at 1161 Hz as well as several harmonics, which are not present in any of the first 10 POD modes.

Moreover, no hydrodynamic structure similar to the ones observed in the inert case can be observed in the first 10 POD modes of the reactive flow. Knowing that the cumulative energy of the first 10 modes accounts for 37.6 % of the total fluctuation energy and that the 10_{th} mode contains only 1.46 % of the total fluctuation energy, this leads to the conclusion that any PVC-like structure present in the reactive flow would have a relatively small impact of the flow

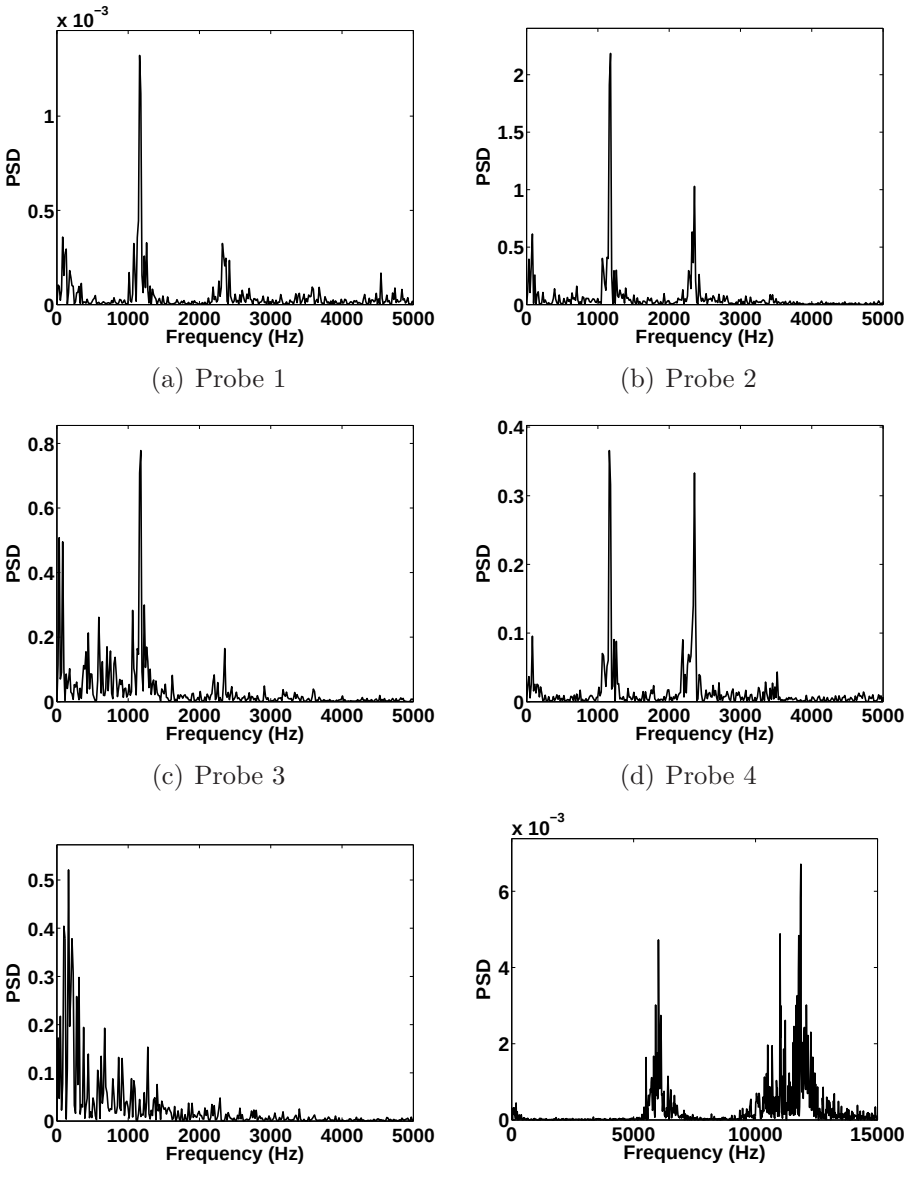

(a) Probe 1 (b) Probe 2

(c) Probe 3 (d) Probe 4

(e) Probe 5 (f) Probe 6

Figure 4.24: Reactive flow of the Injector B. Spectra of the axial velocity at the positions indicated in Fig. 4.16.

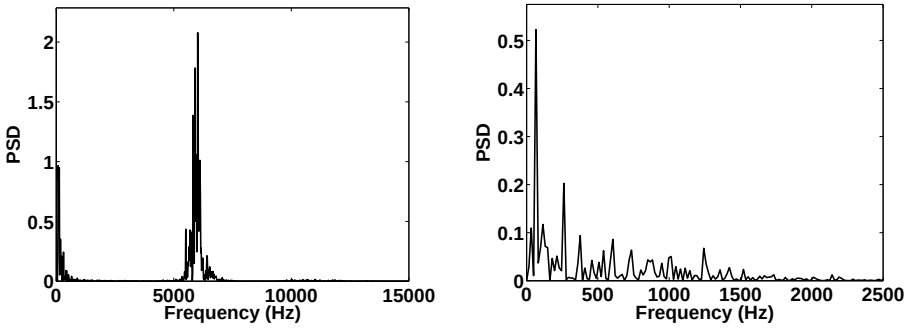

(a) Probe 7

(b) Probe 8

(c) Probe 9

(d) Probe 10

Figure 4.25: Reactive flow of the Injector B. Spectra of the axial velocity at the positions indicated in Fig. 4.16.

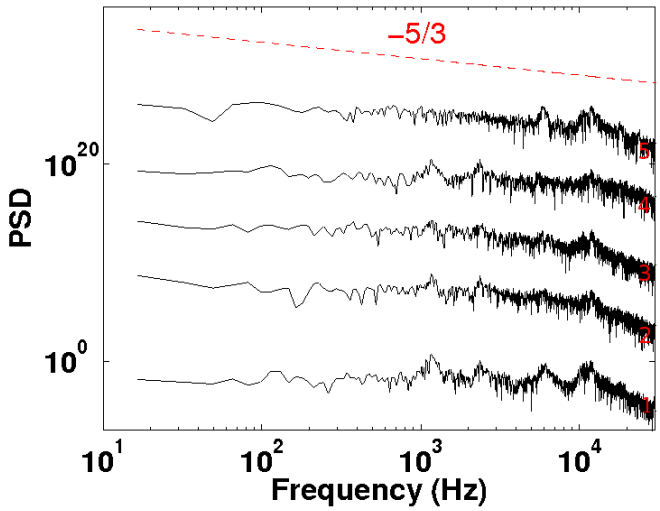

(a)

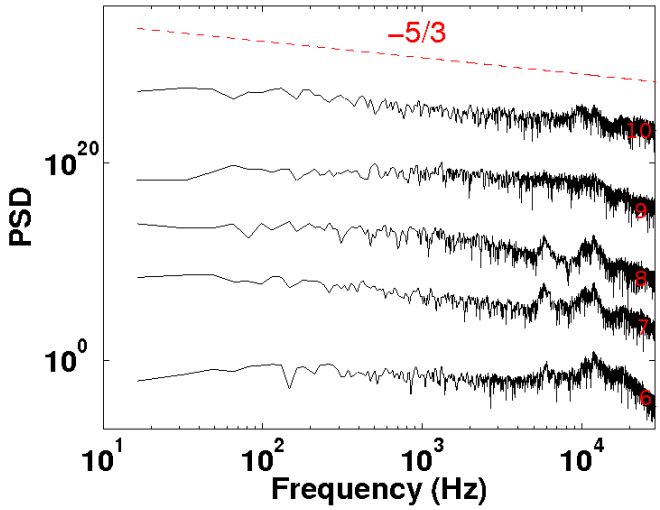

(b)

Figure 4.26: Reactive flow of the Injector B. Spectra in log-log format of the axial velocity at the positions indicated in Fig. 4.16. (a) From bottom to top: points 1 to 5. (b) From bottom to top: points 6 to 10.

fluctuations compared to its inert counterpart. This is also confirmed by the damping of the oscillations that was reported in the velocity spectra analysis. As a result, the interpretation of the modes are more difficult in the reacting case.

It seems that modes 1 and 2 account for the dynamics of a vortex shedding, as revealed by the application of the $Q-$criterion to these two modes (Figs. 5.1(g) and 5.1(h) for mode 1 and mode 2 respectively). However, no commom frequency is observed in their respective spectrum, which would be expected to describe the propagation of the vortex rings. Nevertheless, it can be noticed that one of the frequencies present in mode 2 (32.79 Hz) is a harmonic of one of the frequencies of mode 1 (16.39 Hz), similarly to what can be observed in the POD analysis of the forced bluff body flows in Chapter 4 of Ref. [1]. If we look at the temperature fluctuation contour of mode 1 (Fig. 5.1(g)), the passage of a large vortex ring, as identified by the $Q-$criterion, is found to strongly alter the temperature field of the flame. Here the POD analysis allows to highlight the correlations between different variables such as the velocity and temperature fields.

Another POD computation of the flame has been performed without including the temperature as a POD variable. Its first 10 modes were found to be identical to the ones presented here. Therefore, the absence of the vortical structures that were found in the POD analysis of the inert flow does not seem to be due to the inclusion of the temperature fluctuations field into the POD computation.

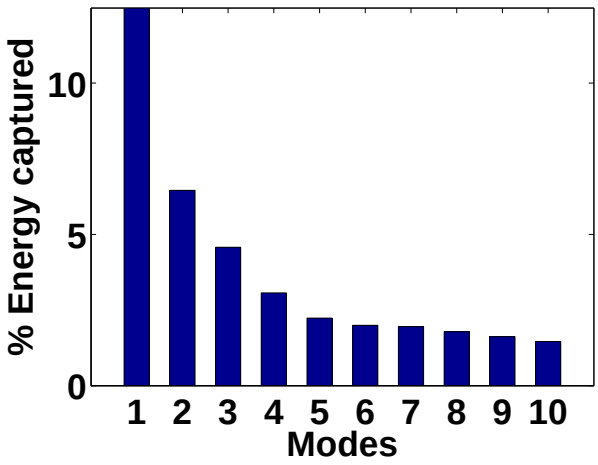

Figure 4.27: Reactive flow of the Injector B. Relative energy contained by each of the first 10 modes.

Chapter 5

Summary of main findings

The Proper Orthogonal Decomposition method applied to the LES datasets of two developmental aero-engine combustors has been found to be a powerful tool in organizing and analyzing the tremendous quantity of information generated by the simulation. In the case of inert combustor flows, the coupled use of POD with LES helps us to identify the vortical structures in the flow and their associated frequencies. This ability is particularly interesting in the case of industrial injectors, which generally feature several swirlers. Thus, in the case of the Injector A, the POD analysis has been able to identify the different Precessing Vortex Cores generated by the different swirlers and to associate a frequency to each of these hydrodynamic structures. The analysis of the injector instabilities and hence the validation of the development injector are therefore much easier, as a direct spectral analysis of the flow would not allow to understand the origin of the different frequency peaks. During the POD computation, the combination of other flow quantities such as the pressure or the mixture fraction in addition to the three velocity components allows a better identification of the important structures of the flow and bring to light the correlation between the vortex precession and the flow mixing, for example.

For the reactive flow of the Injector B, spectral analysis shows that the oscillations present in the inert flow have their frequencies increased, while their amplitudes are largely damped. These observations are confirmed by the POD analysis of the reactive flow, which does not identify any PVC-like structures among the most energetic modes. The presence of high fundamental frequencies

and several of their harmonics in the jets of the different swirlers leads to the conclusion that these instabilities are still present in the reactive flow, although they have been weakened by the combustion process.

Finally, it is interesting to note that the LES/POD analysis of aero-engine injectors have given results that are very consistent with the ones obtained for the TECFLAM academic burner in Chapter 6 of Ref. [1]. This is particularly true in the case of the Injector B where the pilot injector is formed of an annulus located around a bluff body, similarly to the TECFLAM burner.

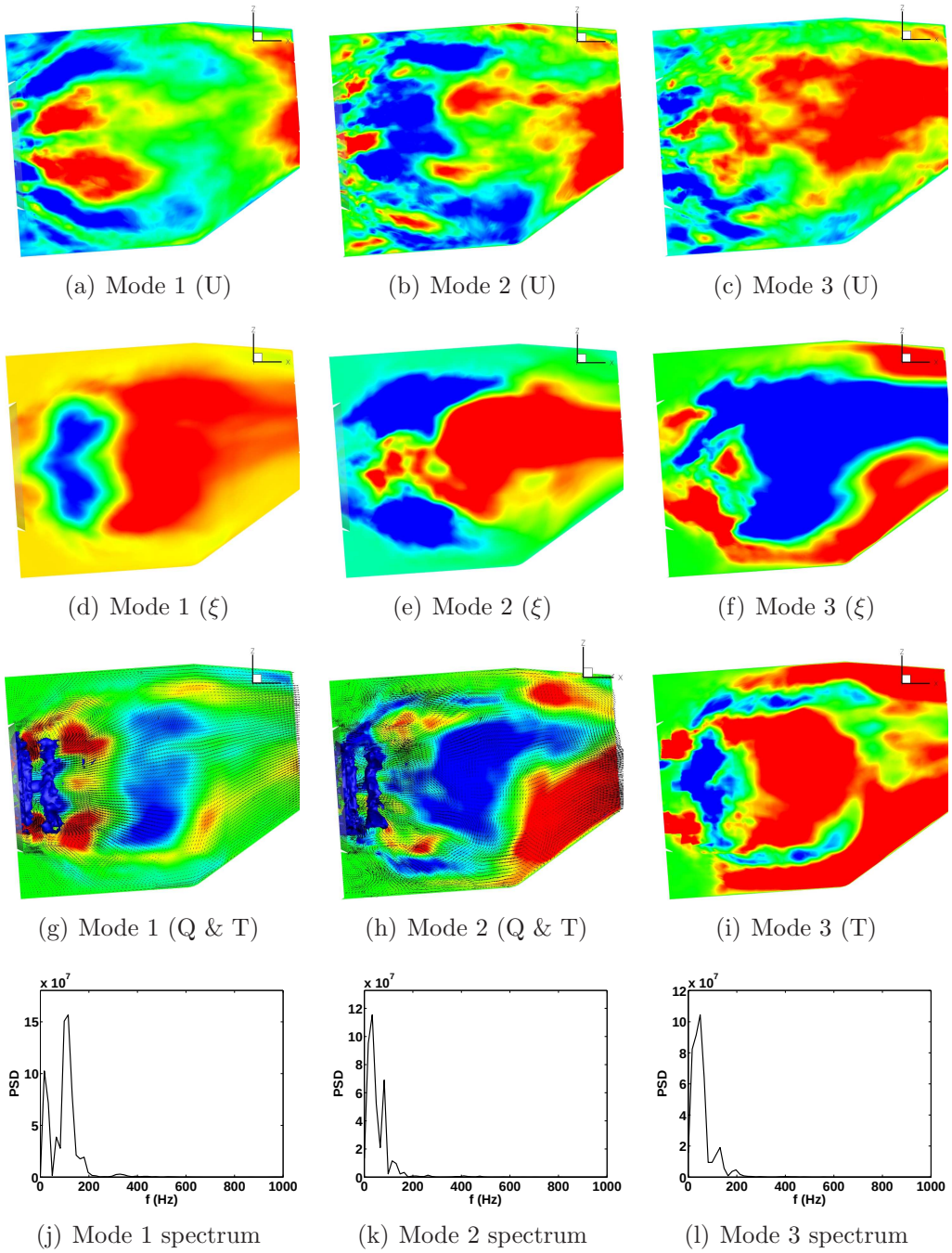

(a) Mode 1 (U) (b) Mode 2 (U) (c) Mode 3 (U)

(d) Mode 1 (ξ) (e) Mode 2 (ξ) (f) Mode 3 (ξ)

(g) Mode 1 (Q & T) (h) Mode 2 (Q & T) (i) Mode 3 (T)

(j) Mode 1 spectrum (k) Mode 2 spectrum (l) Mode 3 spectrum

Figure 5.1: POD modes 1, 2 and 3 from the reactive flow of the Injector B. The spectra refer to the Fourier analysis of the temporal coefficient associated with each mode.

References

[1] S. Ayache. *Simulations of Turbulent Swirl Combustors*. PhD thesis, University of Cambridge, 2012. 4, 9, 29, 30, 34, 39, 42

[2] S. Stow, M. Zedda, A. Triantaffylidis, A. Garmory, E. Mastorakos, and T Mosbach. Conditional moment closure LES modelling of an aero-engine combustor at relight conditions. ASME Turbo Expo 2011, Vancouver, Canada, 6 - 10 June, 2011. 5